ISSN 2277-3061

Finite-Difference Time-Domain (FDTD) Simulation of Novel Terahertz Structures

Yasser Hussein*, Sr. Member IEEE, James E. Spencer**, Sr. Member IEEE, and Samir El-Ghazaly*, Fellow IEEE
Stanford University**, Palo Alto, CA, USA
University of Arkansas, Fayetteville, AR, USA

Abstract

Previous work on compact, variable, efficient, high brightness radiation sources is extended by calculating the radiated power and angular distributions for different configurations and drive sources. Figures of merit are defined in terms of efficiencies or effective impedances such as the radiation coupling impedance Z_r. Characteristics of representative cases are discussed in terms of a few basic parameters. Conditions for interference are discussed and demonstrated. Finally, we discuss some further possibilities together with various impediments to realizing such devices. The differences between bound and free electrons are studied from the standpoint of the frequencies that are practicably achievable. With the ansatz that the transport physics with Maxwell's Equations are valid but modified by the material properties, a number of analogs exist between these two basic sources of radiation. In many cases, the differences are between macro and micro implementations e.g. between klystrons and klystrinos (micro or nano) or solid state and semiconductor lasers or rare-earth doped transistors. Cases with no apparent analogs are ones due to unique quantum effects e.g. radiation at $3kT_c$ in superconductors. This is well above magnetic resonance imaging MRI around 0.4 meV but well below room temperature at 25 meV. Bound and free possibilities for planar, micro undulators over this range are studied using FDTD techniques. To our knowledge, there have been no implementations of either possibility.

Index Terms — FDTD, (sub) millimeter radiation, micro undulators/wigglers, microwave photonics, THz technologies

ISSN 2277-3061

I. Introduction

Previously, we explored possibilities for producing narrow-band THz radiation using either free or bound electrons in micro-undulatory configurations [1]-[4] because integrated circuit technology appeared well matched to this region extending from about 300 GHz to 30 THz. This range [5]-[15] has largely been neglected until recently because it runs from the limit of WR-3 waveguide at 300 GHz up to CO_2 lasers where the laser regime dominates.

The present work is a byproduct of an ongoing goal of making an electro-optic electron accelerator on a chip or AOC. While lasers provide sufficient power, their use generally implies effective cell sizes proportional to their wavelength which poses a major complication. Thus, devices bridging the gap between lasers and conventional RF could prove very useful. Because of their other potential uses [5]-[15], we decided to explore this THz region using wiggler or snake-like configurations such as shown in Fig. 1.

. General Discussion

There are many ways to approach this problem but the most direct is to determine the Poynting vector based on calculating the acceleration fields in the far field and from it the angular distribution:

$$\frac{d\boldsymbol{P}}{d\Omega} = \frac{1}{4\pi c^3}\left\{ \hat{n} \times \int \frac{\partial \boldsymbol{J}(\boldsymbol{r}', t_r)}{\partial t} d\boldsymbol{r}' \right\}^2 \quad \textbf{(1)}$$

For β <<1, the above relation reduces to:

$$\frac{d\boldsymbol{P}}{d\Omega} = \frac{e^2}{4\pi c^3}\left\{ \frac{\partial \boldsymbol{v}(t)}{\partial t} \right\}^2 \sin^2(\theta) \quad (2)$$

Where θ is the angle between the observation direction $\hat{n}$ and the direction of acceleration at emission time *t*.

An important aspect of any source is the ability to measure it so we place a high value on reciprocity. Fast switching transistors or the production of x-rays via electron bremsstrahlung are classic examples of the inverse of the photoelectric effect that is used to produce electrons when the photon energy $h\nu$ has an energy sufficient to assist the electron in overcoming the Schottky barrier. The phase space densities of the resulting electron or photon beams depend on their wave vectors and both beams will diverge/diffract without confining potentials or guide structures that are properly matched to the incident beams. These are the reasons for the increased use of laser driven, RF assisted electron guns and photonic band gap crystals.

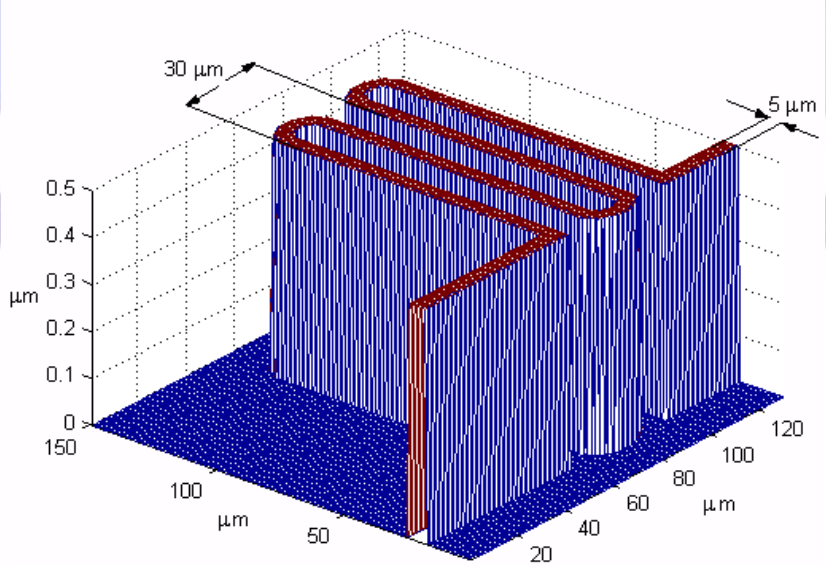

Fig. 1. Planar lattice (not to scale) for 1.5 periods of a 2-D wiggler with the vertical representing a perfect conductor of 0.5 microns thickness and "0" a dielectric substrate (Duriod: relative permittivity of 2**.2).**

If one runs the resulting beam of free electrons into a macroscopic undulator [16] having a wavelength λ_U they will radiate at harmonics *n* of the device period:

$$\lambda \sim \frac{\lambda_U}{2n\gamma^2} \tag{3}$$

where the electron energy γ is in units of rest mass mc^2. Clearly, one can benefit from increasing the energy or reducing λ_U or the effective mass m* (making γ a tensor makes m an invariant). For low energy conduction band electrons, $\gamma \sim 1$ so that a wiggle period of $\lambda_U = 60\,\mu$m achievable with standard IC techniques, might be expected to give 30 μm, 10 THz radiation. We explore the validity of these ideas and ways to implement such devices.

III. FDTD Code Validation

Finite Difference Time Domain (FDTD) is a powerful and flexible technique that is expected to play a central role in development and simulation of sub-millimeter wave devices. It was chosen over others because it is very efficient and its implementation is straightforward. Also, the FDTD method is ideal for our problem which is non-linear and may include anisotropy.

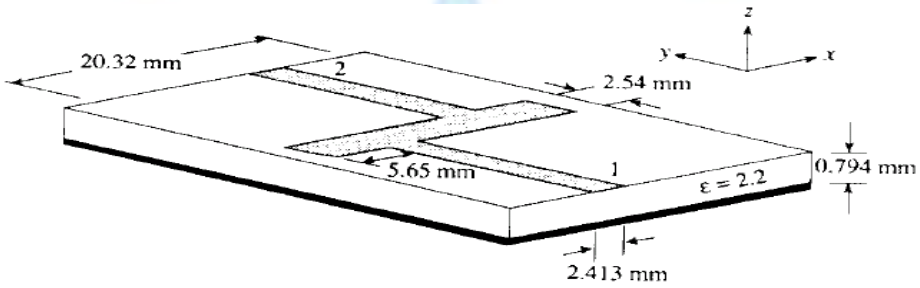

Fig. 2. Bench-mark filter used to validate the FDTD code.

Before presenting simulation results for any undulators, the developed FDTD code should be validated. The results are compared to those presented in [17]. The low-pass filter used to validate the code is shown in Fig. 2. Comparison results for the insertion loss (S_{21}) and return loss (S_{11}) are shown in Figs. 3 and 4. One observes good agreement with measured and calculated data except for the highest frequency which is somewhat shifted. Experimentation with planar circuit techniques leads one to conclude that this shift is caused mainly by the slight misplacement of the ports inherent in the choice of the spatial steps [17].

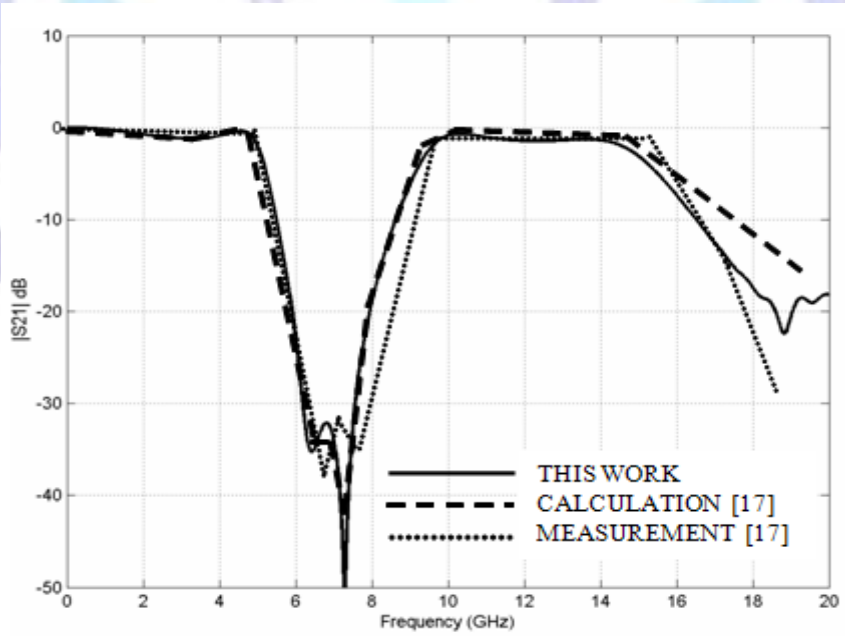

Fig. 3. Insertion loss comparison curves of the low-pass filter.

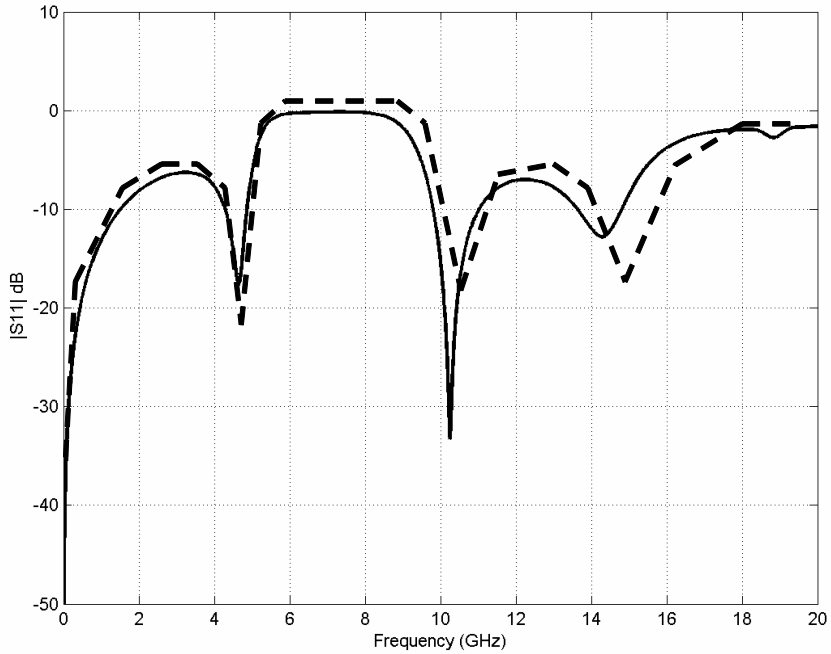

Fig. 4. Return loss comparison curves of the low-pass filter

IV. Illustrative Examples

Figure 1 shows a sample, planar lattice for 1.5 periods of a two-dimensional (2-D) wiggler. Several examples of these structures have been printed with different periods and wavelengths [18] where dimensions were scaled to give the same low frequency impedances for similar periods. Pulse currents greater than 1 A at 1 ns were obtained routinely without failures by careful conditioning.

Different 2-D and 3-D implementations are interesting to pursue as well as other inductor-like topologies or laser driven, high mobility, direct band gap materials but first, it is useful to check the consistency between the classical and microscopic pictures we have assumed.

For conventional synchrotron radiation [19], one can estimate an energy loss per wiggle turn of:

$$U(\mathrm{meV}) = \frac{3.0\gamma^4}{\rho(\mu)} \tag{4}$$

where □ (□) is the bend radius in □ m We note that Eq. (2) can be due to magnetic or other equivalent effects because any change in velocity or momentum of an electric charge results in radiation. Further, the average photon energy u can be written:

$$< u(\mathrm{meV}) > = \frac{94.3\,\gamma^3}{\rho(\mu)} = 9.5 \tag{5}$$

where we have assumed a radius of 10 □ m from Fig. 1. For reference, a 0.5 THz photon has an energy of □ 5 meV. Thus, the assumption of constant □ in Eqs. (4)-(5) appears reasonable, ignoring intrinsic scattering in the material.

V. Results And Discussion

FDTD simulations were carried out for wiggler structures such as shown in Fig. 1 for 1.5 periods. The half-period circuit length L is 231.4 □m for □$_U$=30 □m. This gives a fundamental resonant frequency f_0 of 0.437 THz. This is not f_U for a free electron from Eq. (1). The return loss for a half period and 1.5 periods are shown in Figs. 5 and 6 normalized to the frequency f_0. None of these structures, in this form, are expected to be coherent.

Figure 5 demonstrates that an electron wave passes through the structure with very small reflection at f_0 because it doesn't resolve the half loop well at this frequency and so passes through it with virtually no reflection. Further, the broad reflections around 2, 4, 6, and 8 f_0 are due to harmonics of the reflection coming from the loop at ¼ of the wiggler period. As the frequency increases, the reflection coefficient increases and broadens consistent with the fact that higher frequencies resolve and sample the full loop better. From Fig. 1, Eqs. (3)-(4) and f_0 we expect a radiation rate of □ 0.03 photons per electron per half loop with a diffuse pattern based on a mean angular spread of □ 1/□ radians. While not optimal for brightness, it does imply out-of-plane radiation. We also expect the reflected electrons to radiate photons with a different radiation pattern in a competitive way because □ □.ı

In Fig. 6, there are three small reflections around f_0 corresponding to the same mechanism as in Fig. 5 before one reaches the strong first loop reflection at the same frequency as for Fig. 5. For coherence with such structures we would require multi-port feeds. In such cases, one could expect the three peaks to merge at f_0 with a more pronounced resonance structure. Another observation is that the broad reflections around 2, 4, 6, and 8 f_0 exist also for the 1.5 period case except there are now loops at ¼, ¾ etc. of the wiggler period. This explains why these reflections for the 1.5 period case are higher than the half period case by direct analogy with HR coatings.

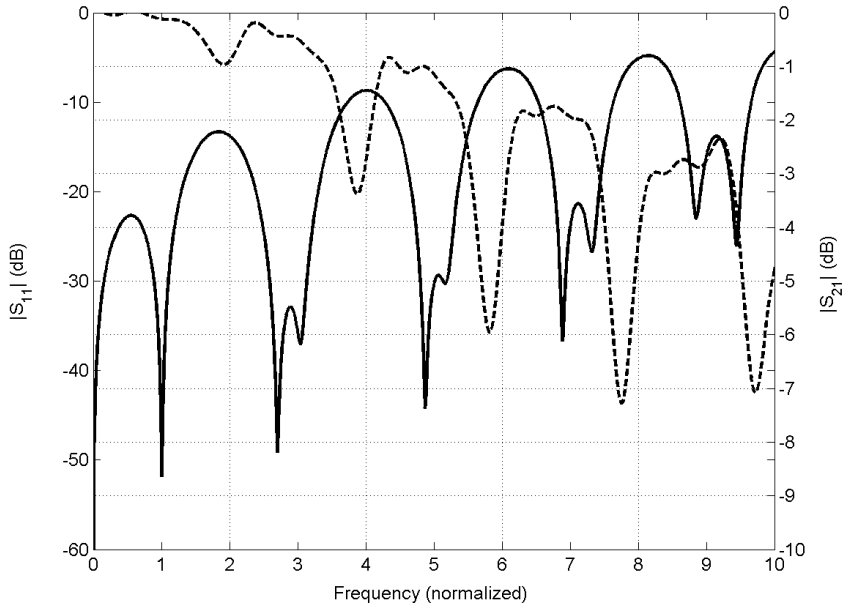

Fig. 5. Insertion and return loss versus f / f_0 for the 0.5 period wiggler.

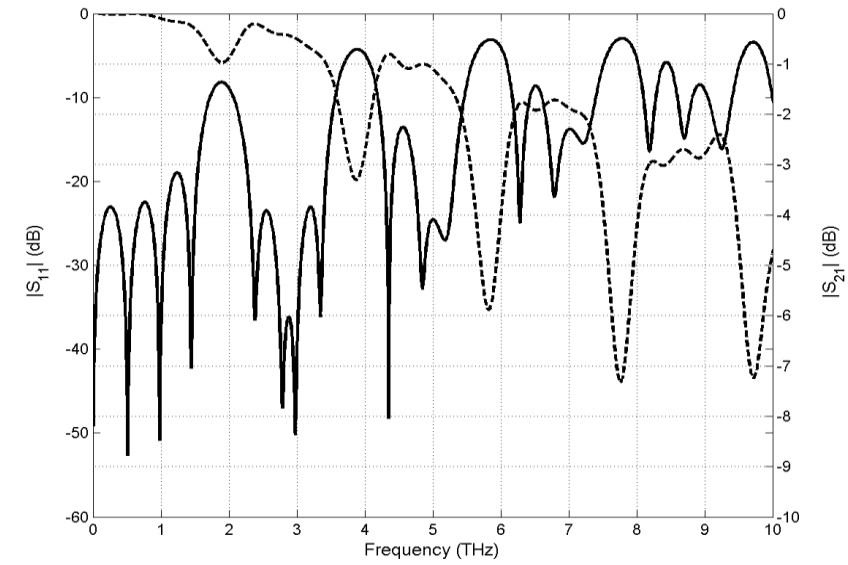

Fig. 6. Insertion and return loss versus f / f_0 for the 1.5 period wiggler.

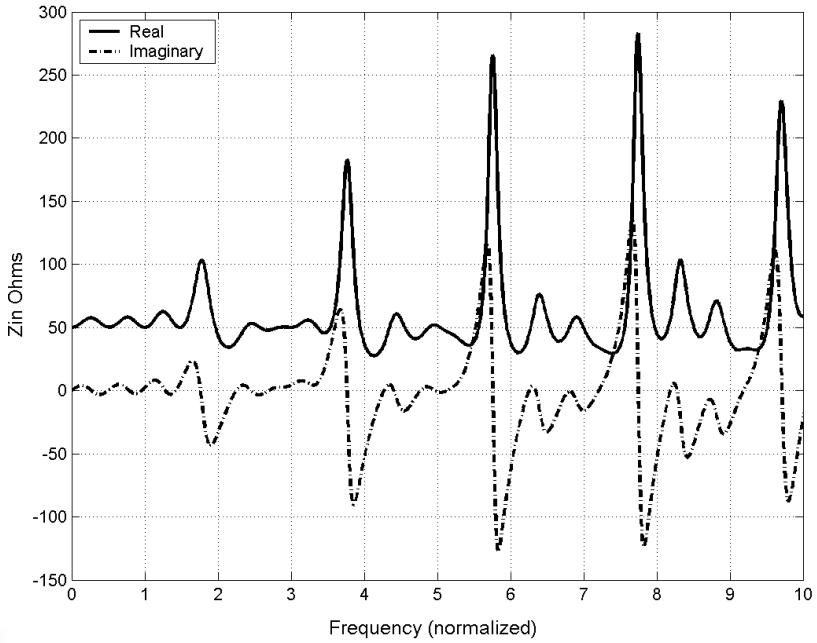

Fig. 7. Input impedance versus f / f_0 for the 1.5 period wiggler.

Figure 6 shows also the insertion loss versus frequency for 1.5 periods. As the frequency increases, transmission decreases. This is dual to the return loss parameter. Figure 7 shows the input impedance (real and imaginary) as a function of frequency. At deep resonance, the input impedances are purely real (50Ω). This corresponds to a matching load that has zero reflection. Under the assumption of ballistic transport, this implies a broad band radiation spectrum having the mean energy given by Eq. (5) although such radiative losses are not explicitly reflected in these plots.

On the other hand, the broad reflections around 2, 4, 6, and 8 f_0 have higher values of input impedance (mismatching) emphasizing that many more electrons are reflected at these frequencies producing radiation with a more bremsstrahlung-like spectrum. This mode relates most closely to IMPATT devices. In both cases, ballistic transport and reflection, the spectra and distribution patterns are expected to be very different with the latter extending to higher frequencies and in lowest order having a dipole distribution whose axis is centered on the incident electron's wave vector so the radiation peaks in directions around the perpendicular to this vector. This is in direct contrast to the synchrotron-like radiation. With increasing frequencies we expect such differences to become better defined because the classical conditions for radiation [19] improve.

To obtain a bound, micro undulator that retains the 2-D structure of Fig. 1, we can add a thin covering dielectric layer followed by a broad strip of metal running perpendicular to the straight segments as shown in Fig. 8. This is pulsed with shorter duration, higher peak currents that couple to the fields of the previous circuit to produce coherent radiation (Eq. 1) whose wavelength varies with the angle of observation relative to the oscillation plane. This relates to Smith Purcell radiation [20] but is more practical. There are many variants. For the free case one can add a mirror symmetric circuit above Fig. 1.

A useful figure-of-merit for such devices is the 6-D, normalized brightness in the form of a photon density:

$$B_n^6 = (4\pi)^2 \frac{\mathrm{N}_\gamma}{\lambda^2 \sigma_t \sigma_\omega / \varpi} \eta \le 7 \cdot 10^{16} \eta / \lambda^3. \tag{6}$$

Even for η«1, bound implementations are far preferable since this is an intense source by virtually any standard. Even the differing uses of metals in such devices, as opposed to semiconductors, is too broad to discuss here as well as the differences between metals such as Al and Au for use in fast laser drive systems [2] but we would be remiss to not mention materials such as poled, periodic lithium niobate [22] that could also be used with electrons.

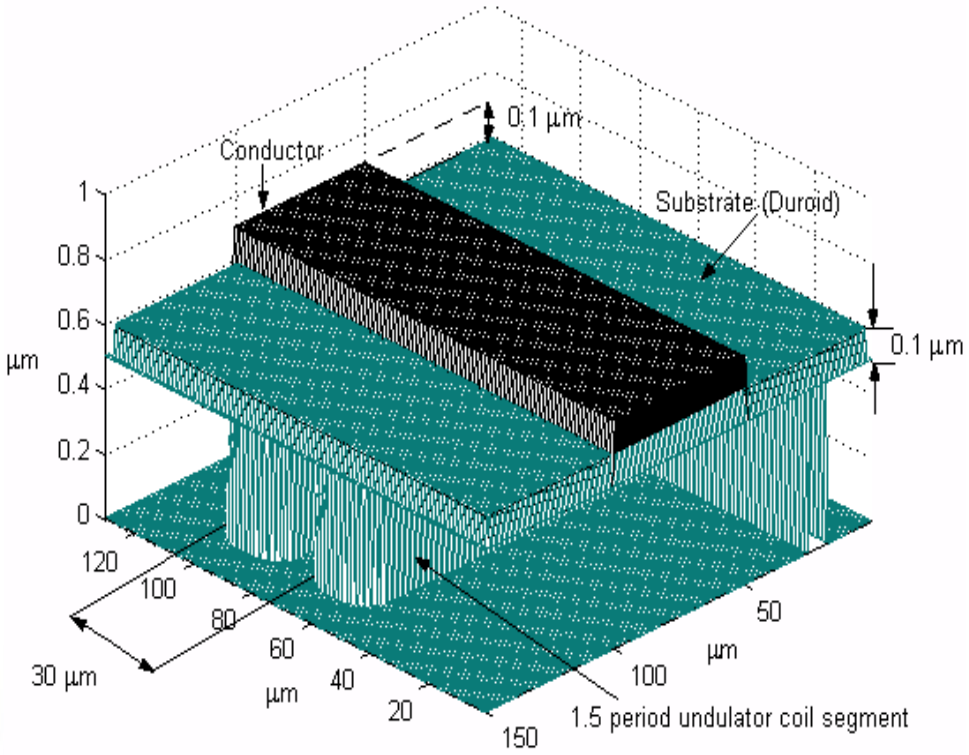

Fig. 8. 1.5 period segment of a 2-D undulator based on Fig.1.

In a typical, 2-port, lossy, microwave structure, the power dissipated (normalized to the input power) can be estimated on the assumption that the S-matrix is complex and orthogonal as:

.

$$P_l = 1 - |S_{11}|^2 - |S_{21}|^2 \geq 0. \quad (7)$$

The power dissipated can be due to radiation, conductor, or substrate loss. For instance, for a standard radiating structure with no output port (S_{21}=0), the dissipated power is dependent on S_{11} only. In this case, small values of S_{11} indicate high loss. Further, if we assume no conductor or substrate loss, the radiated power must go inversely as $|S_{11}|^2$. If we define radiation efficiency as:

$$\eta = \frac{P_r}{P_l} \quad (8)$$

Then this radiating structure has 100% radiation efficiency since all the power dissipated is due to radiation. If a second port exists, the dissipated power must depend on the transmission coefficient as well (S_{21}), with higher transmission indicating lower losses. In addition, if part of the dissipated power is due to substrate and/or conductor loss, the radiation efficiency in this case, based on (2), will be less than 100%. An example of this is the half-period wiggler where a portion of the loss is dissipated in the substrate (the substrate is assumed to be lossy with a small loss tangent value). Another definition for the radiation efficiency can be given as:

$$\eta = \frac{P_r}{P_t} \quad (9)$$

where P_t is the total power applied to the structure. This definition states that the efficiency is the percentage of power lost into radiation compared to the total power applied to the structure-ideally the so-called wall-plug power.

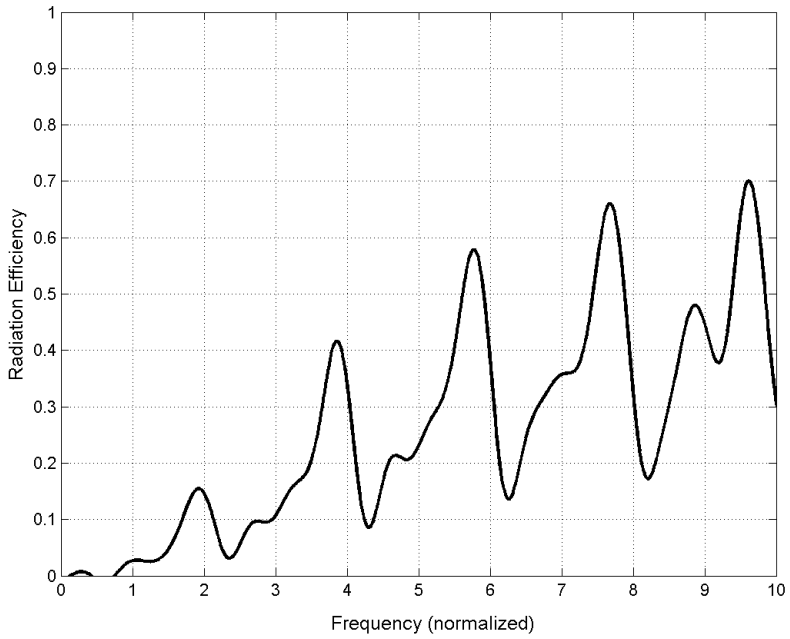

Fig. 9. Radiation efficiency from Eq. (9) versus f / f_0 for the 0.5 period wiggler

Fig. 9 shows the radiation efficiency as a function of the normalized frequency for the half-period wiggler. One observes that the radiation efficiency increases with frequency. In addition, the radiation efficiency maxima track the minimum of S_{21}, which occur around 2, 4, 6, 8, and 10 f_0 as discussed above. It is noteworthy to underline that the resonant frequencies are estimated based on a constant relative permittivity. This explains the results in the previous figures, where the high resonant frequency values are overestimated because the effect of the increase of relative permittivity with frequency is not included. A simple estimate for the relative permittivity at 10 f_0 gives ~ 1.1 ε (f_0).

HFSS simulations were carried out to calculate the radiation pattern of the half-period period. Fig. 10 shows the radiation pattern at Phi=90 (the YZ plane) for different frequencies, with the angle theta starting from the –y axis. One observes that higher frequencies have higher radiated power while S_{11} trends higher while S_{21} decreases with frequency. Because the value of S_{21} (close to unity) is higher than S_{11} (close to zero), the radiated power tracks S_{21}. Further, at high frequency and looking at the YZ plane, the half-period wiggler acts as a dipole antenna; the EM-waves propagating along the different sides of the half-period wiggler have different directions. Moreover, the 90-degree turn generates radiation at high-frequency. These were put in to avoid crosstalk between input and output ports and also a well-defined loop was required to study at this stage of the work. This explains the radiation pattern of Fig.10, where a second loop is partially created at higher frequency. On the other hand, Fig. 11 shows the radiation pattern at Phi=0 (the XZ plane) for different frequencies, with the angle theta starting from the –x axis. One observes again that the radiated power increases with frequency. Further, the radiation pattern is unsymmetrical. Considering Fig. 11, one concludes that the half-period wiggler is equivalent to a dipole antenna resting at a certain angle in the XY plane, and this angle depends on the operating frequency.

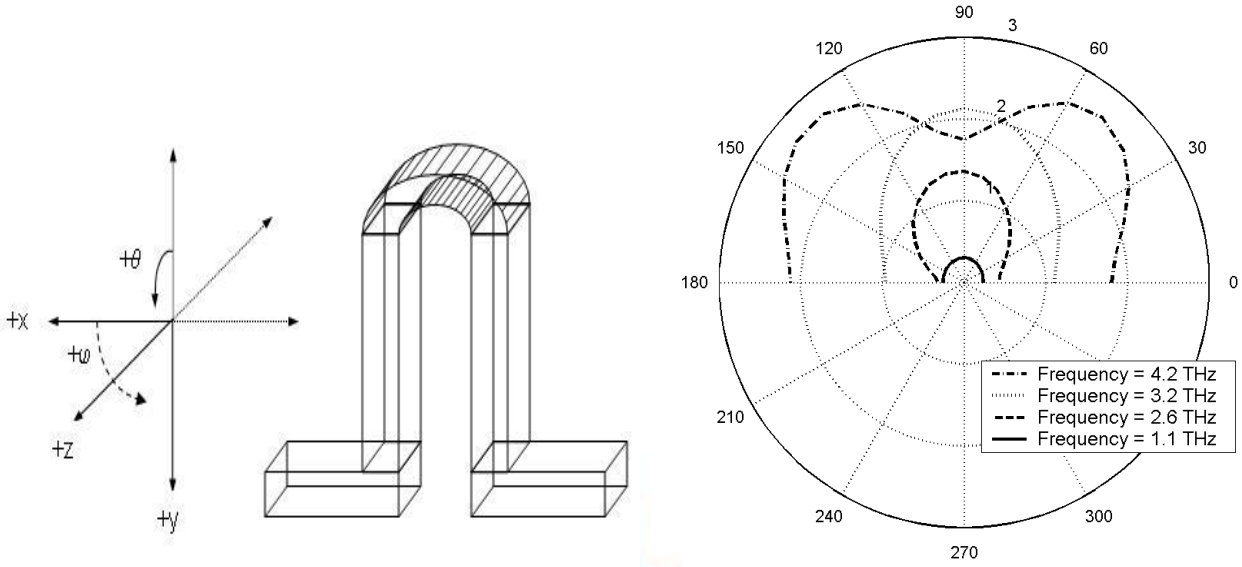

Fig. 10. Radiation pattern for the total electric field at Phi = 90 for different frequencies.

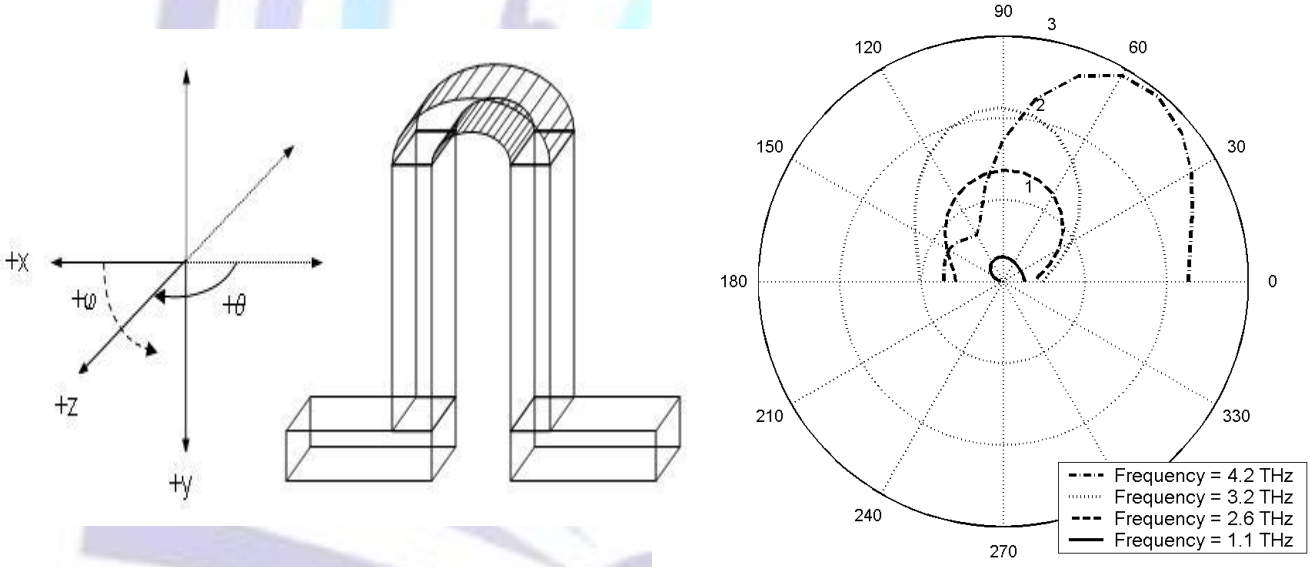

Fig. 11 Radiation pattern for the total electric field at Phi = 0 for different frequencies.

To further investigate the characteristics of the half-period wiggler, the lengths of the two transmission lines (T) at either side of the wiggler are varied so that the half-circle is connected to the ports via transmission lines of length T. As a result, the first resonant frequency should occur at a higher/lower frequency, which can be checked by looking at the S-parameters curves, Figs. 13 and 14. It is worth noting that the purpose of reducing the length T is to have radiation at higher frequencies and also to achieve a more pure dipole-like radiation pattern at these frequencies.

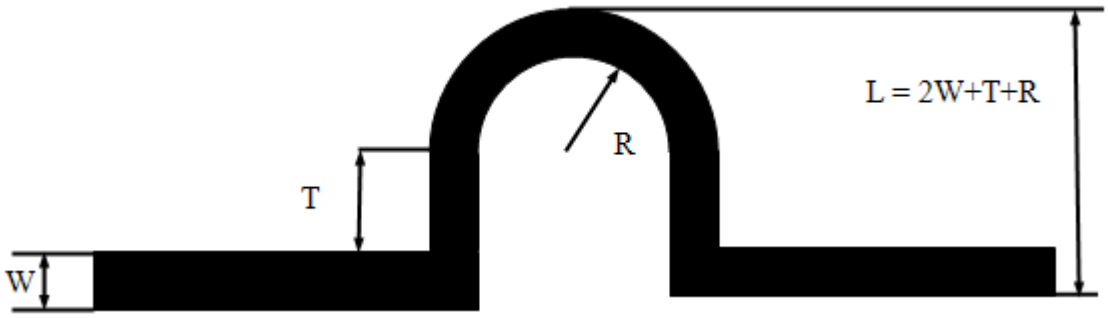

Fig. 12. Top-view of the 0.5 period case. R = 4 μm, W= 2 μm, and T takes values (0, 2, and 3.2 μm).

It is found that the resonant frequencies for planar circuits follow Eq. (10):

$$f_{l,m} = \frac{c}{\sqrt{\in_{eff}}}\sqrt{\frac{l^2}{(2a)^2}+\frac{m^2}{(2b)^2}} \tag{10}$$

where a = L = 2W+T+R and b = πR+ 2T. $\in_{eff}$ is the effective permittivity, which is a function of frequency. Further, the effective relative permittivity equals to ~ 2.2, 1.96, and 1.32 for the modes $f_{0,1}$, $f_{1,0}$, $f_{1,1}$, respectively. This is consistent with the fact that the more complex the mode, the more field lines are in air compared to the substrate resulting in a smaller values of $\in_{eff}$. Figs. 13-14 show the return and insertion loss as a function of frequency for the different cases. One observes there is good agreement between the resonant frequency values obtained using the FDTD code and Eq. (10).

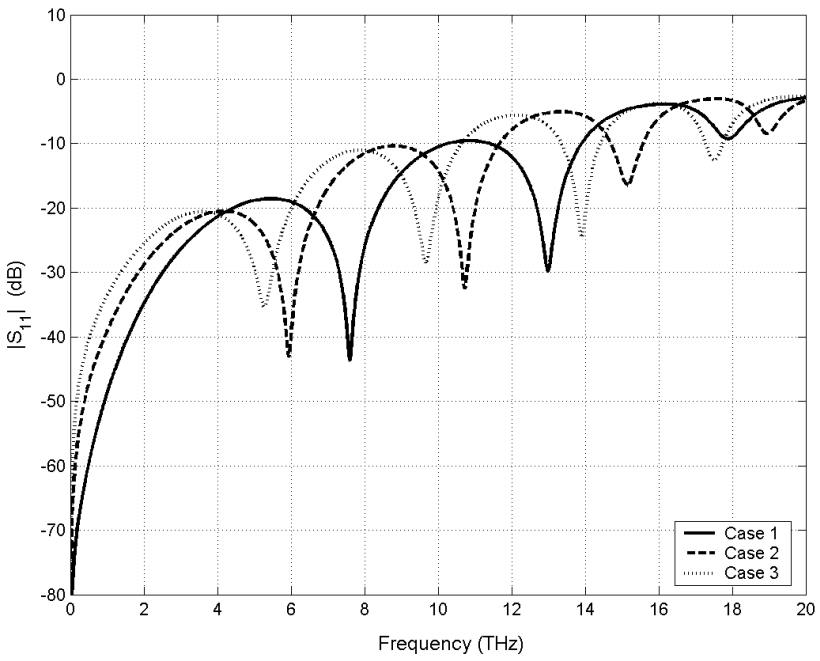

Fig. 13. Return loss versus frequency for the half-period wiggler shown in Fig. (13). Case 1: T= 0 μm. Case 2: T= 2 μm. Case 3: T= 3.2 μm.

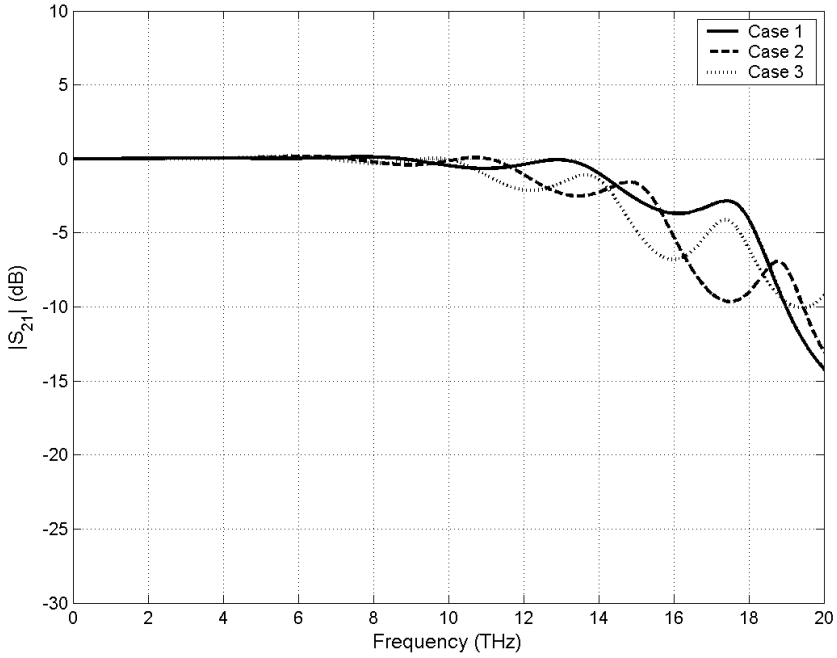

Fig. 14. Insertion loss versus frequency for the half-period wiggler shown in Fig. (13). Case 1: T= 0 μm. Case 2: T= 2 μm. Case 3: T= 3.2 μm.

HFSS simulations were carried out to calculate the radiation pattern of case 1- provided in Fig. (12). The radiation patterns for phi equals to 0 and 90 degrees are shown in Figs. 15 and 16. Considering Fig. 16 and at *f* = 4.0 THz, one notices that the radiation pattern is more symmetric and have a dipole-like radiation pattern. This is in contrast to the original wiggler (Fig. 10), where at 4.2 THz the radiation pattern is distorted, i.e. has bad directivity. Moreover, one notices that the radiation pattern at phi equals to 0 degree for *f* = 4.0 THz is not symmetric simply because the XZ plane identifies the distance between the input and output transmission lines. One observes also that tradeoffs exist between the radiation efficiency and directivity. This is noticeable by considering the peak values of the radiated electric fields, which show that the efficiency of the original case is higher than the case provided in Fig. (12) that has the better directivity. Figs. 17 shows the 3D radiation patterns at different frequencies. One observes that at *f* = 18 THz, the radiation pattern is distorted. This is due to the high-frequency radiation coming out of the sharp edge connecting the port to the half-circle.

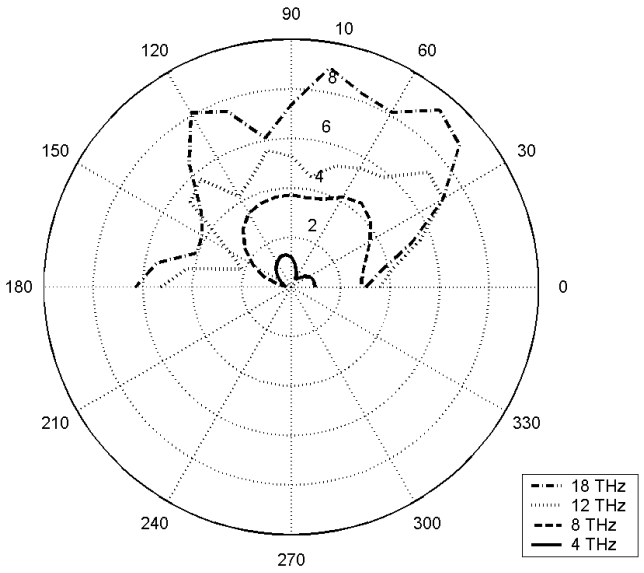

Fig. 15 Radiation pattern for the total electric field at Phi = 0 for different frequencies

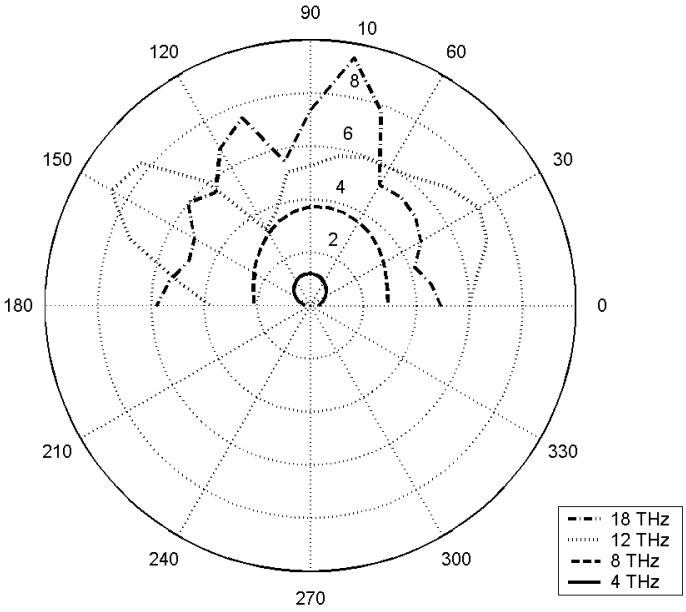

Fig. 16 Radiation pattern for the total electric field at Phi = 90 for different frequencies

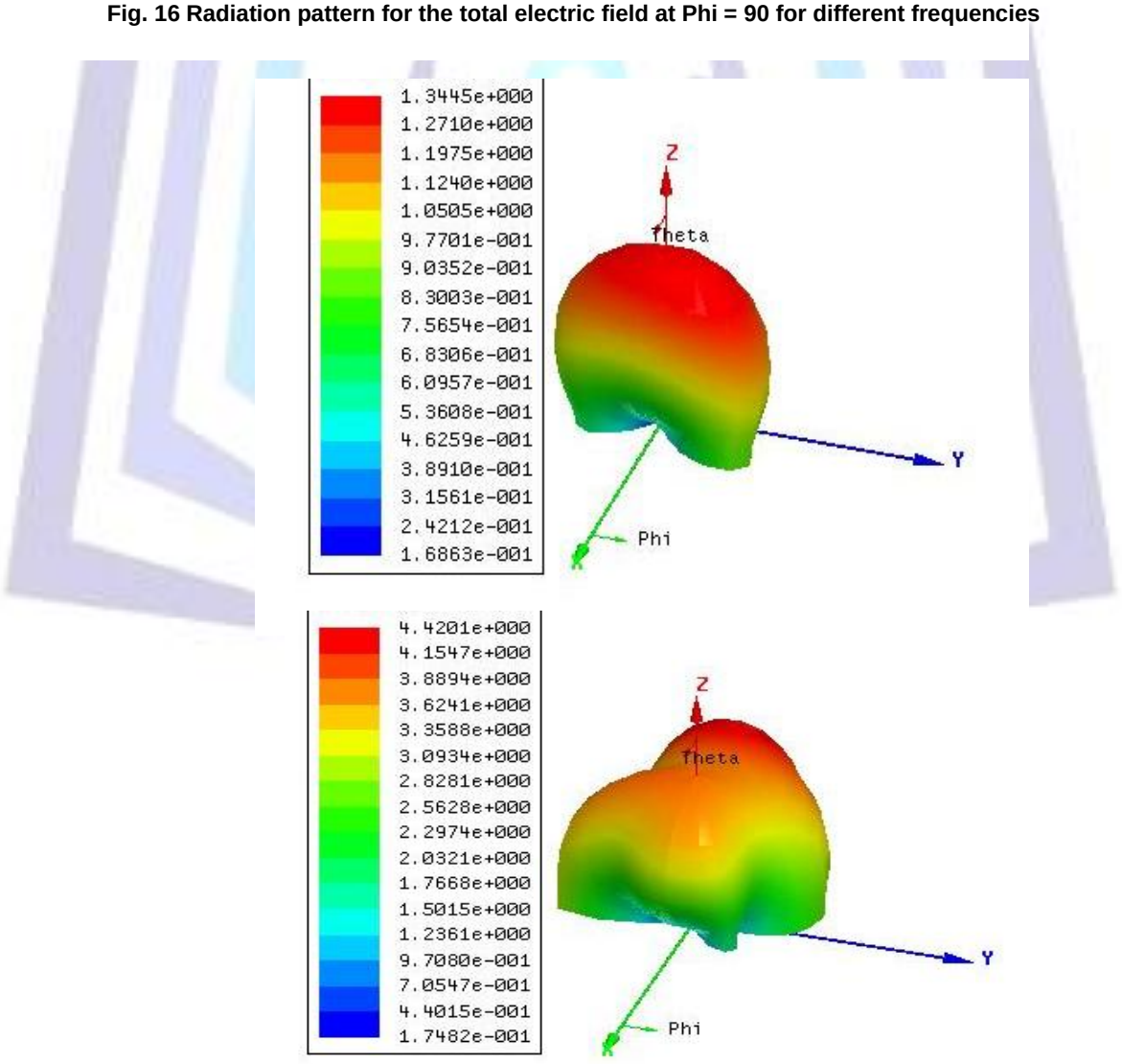

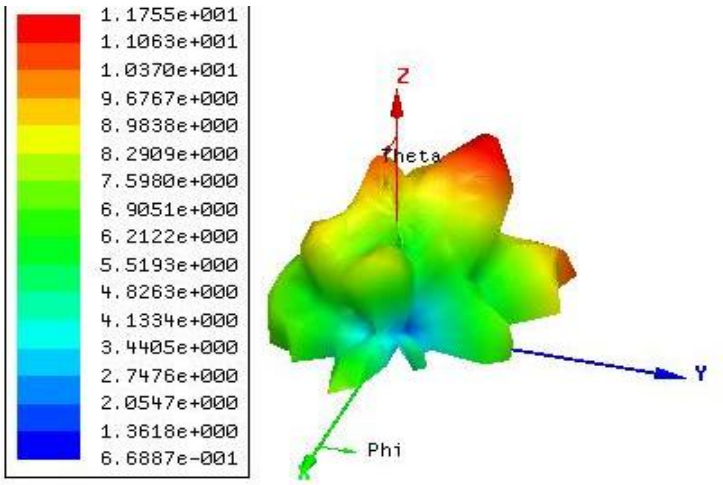

Fig. 17. 3-D radiation pattern (mV) at 4, 8, and 18 THz

In this section, a second half circle is added to the first one on the same transmission line with one facing up and the other down. The return and insertion loss are shown in Figs. 18 and 19. One observes that a new resonant frequency is created at 3.8 THz, which corresponds to twice the wavelength of a single half-circle (7.9 THz). Good agreement between the results obtained by the FDTD code and HFSS can also be conferred. Moreover, the number of resonant frequencies is doubled in the same frequency range. Fig. 20 shows the radiation efficiency versus frequency for three different cases. It can be seen that the radiation efficiency is increased because there are two half-circles radiating instead of one. In addition, the radiation efficiency is roughly quadrupled at 16 THz-indicating coherence at this frequency. Also, for the case without kinks, the radiation efficiency increases almost linearly, and coherence is not achieved because the loops are not well-defined. Finally, considering the radiation patterns for both the half-circle and two half-circles, one concludes that the directivity of the second case is much better. This is in analogy with an antenna array, i.e., a two-element array antenna has better directivity than that of a single element antenna.

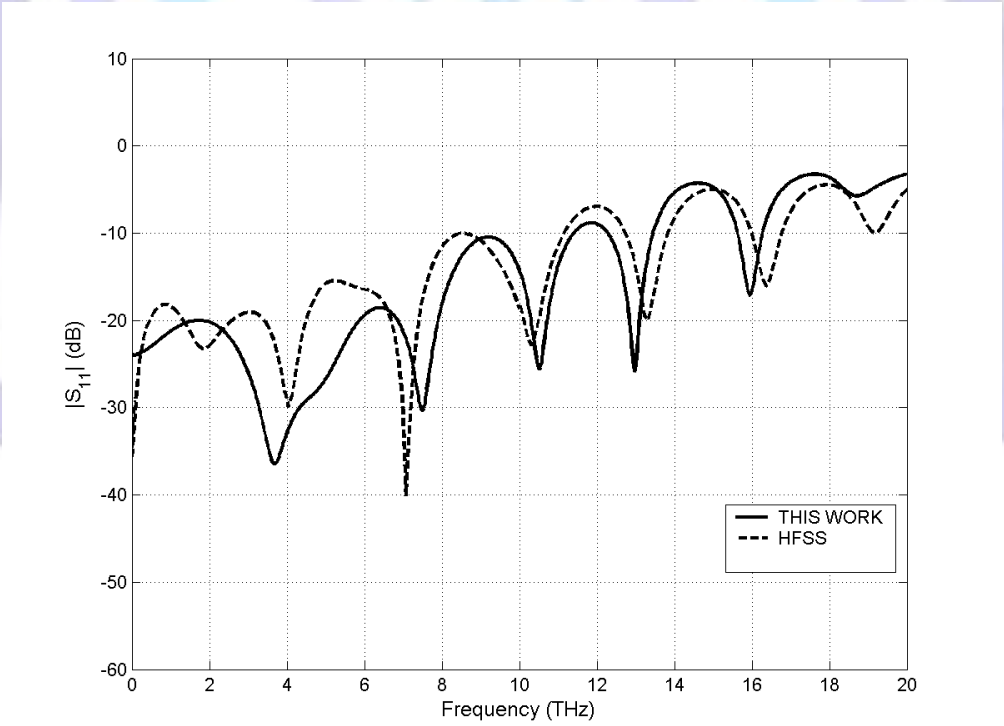

Fig. 18. Return loss versus frequency.

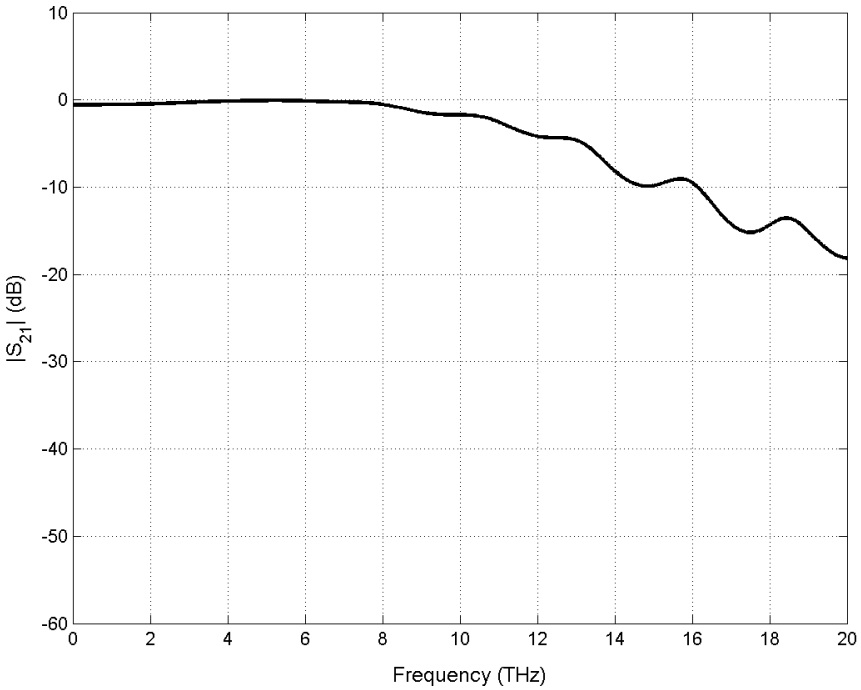

Fig. 19. Insertion loss versus frequency.

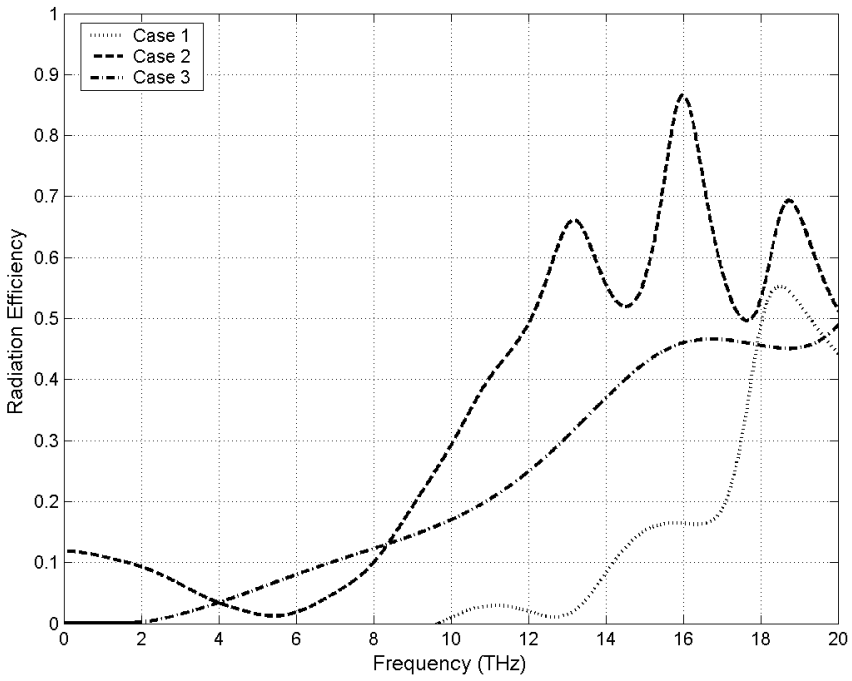

Fig. 20. Radiation efficiency curves for three cases. Case 1: one half-circle. Case 2: two half-circles. Case 3: two half-circles without kinks.

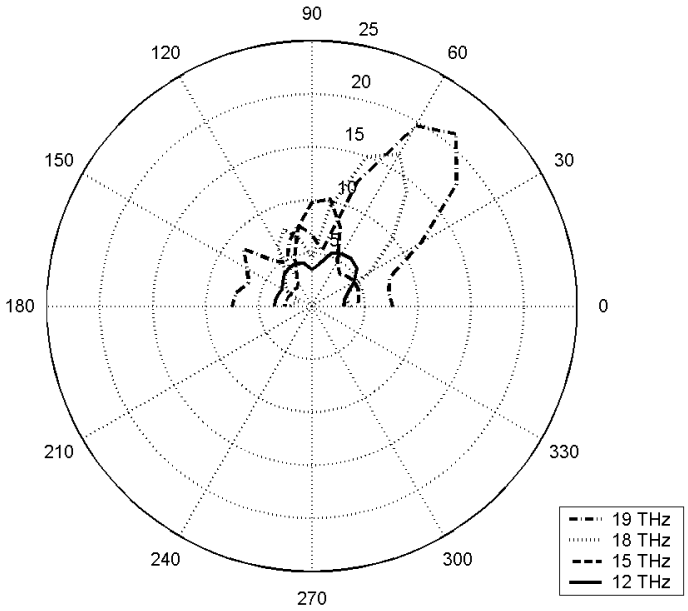

Fig. 21. Radiation pattern for the total electric field at Phi = 0 for different frequencies

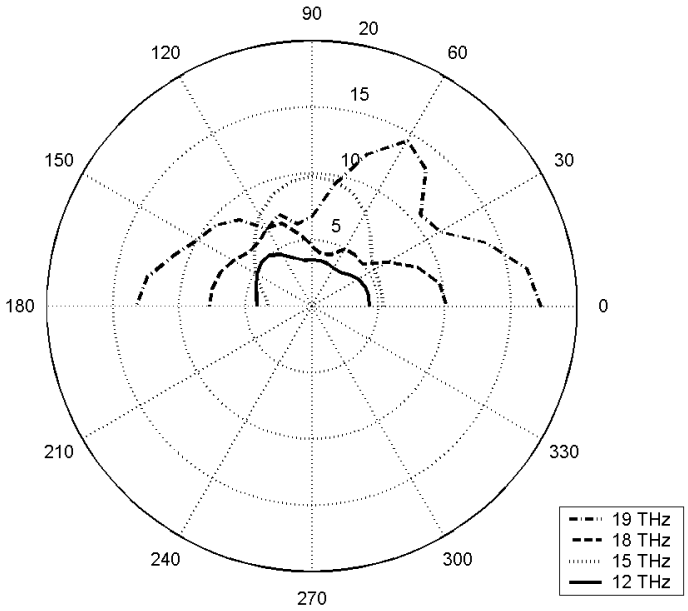

Fig. 22. Radiation pattern for the total electric field at Phi = 90 for different frequencies

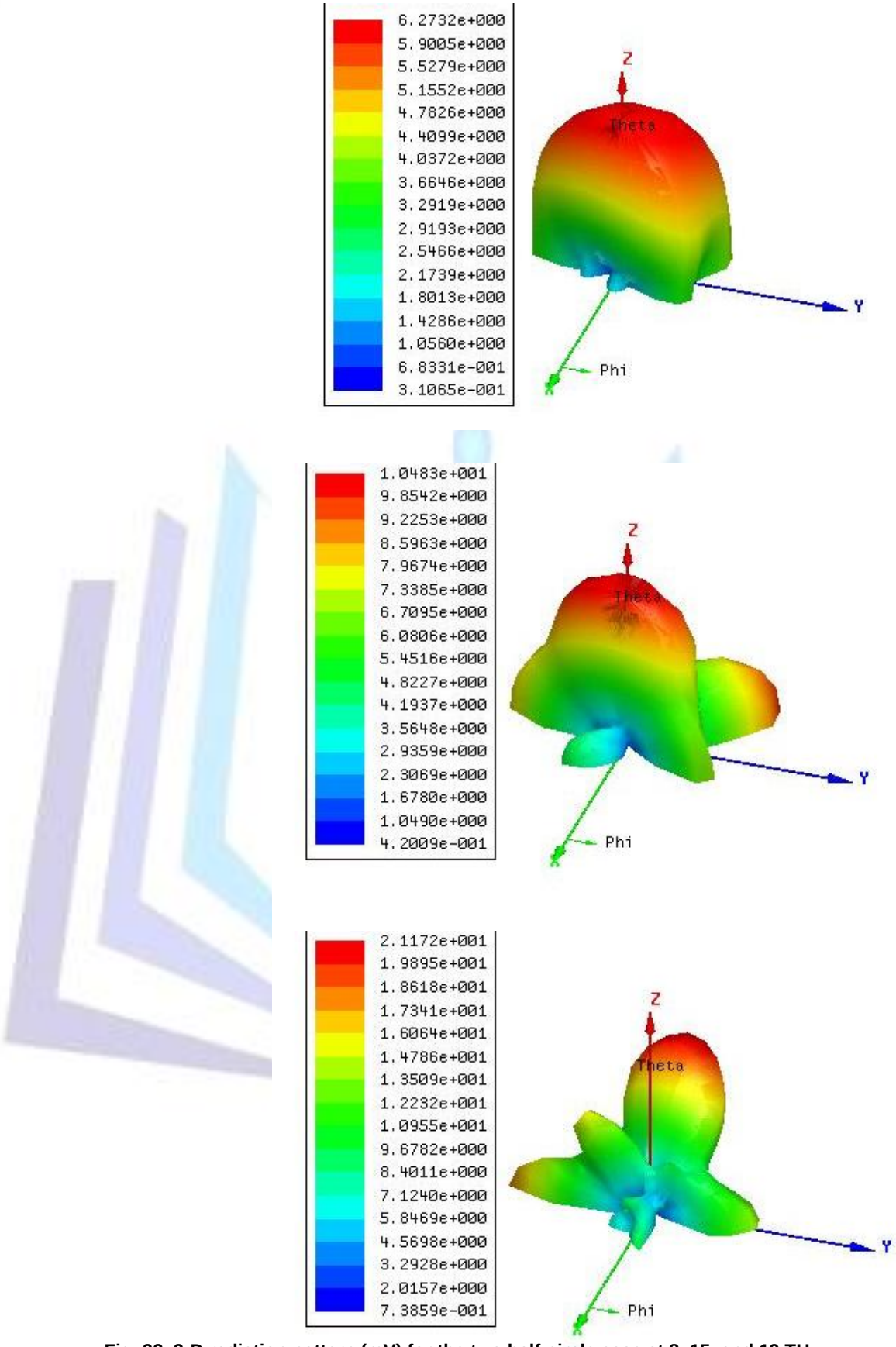

Fig. 23. 3-D radiation pattern (mV) for the two half-circle case at 8, 15, and 19 THz.

Another figure of merit to characterize a radiating structure is the radiation coupling impedance:

$$Z_{rc} = \frac{|E_{peak}\lambda|^2}{P_{total}} \quad (\Omega) \tag{10}$$

ISSN 2277-3061

TABLE I

COMPARISON OF COUPLING IMPEDANCE FOR DIFFERENT CASES

Frequency (THz)	$\lvert E_{peak}\lambda \rvert$ (One Half Circle)	$\lvert E_{peak}\lambda \rvert$ (Two Half Circles)	Z_{rc} (Ω) (One Half Circle)	Z_{rc} (Ω) (Two Half Circles)
2	0.41	0.45	0.16	0.20
4	1.33	1.57	1.76	2.46
8	4.42	6.23	19.53	38.81
12	8.65	5.8	74.82	33.64
15	9.37	10.25	87.79	105.06
18	9.47	16.55	89.6	273.90

The coupling impedance is a measure of how much power is lost into radiation. Table I emphasizes that radiation coming out of the two half circles is higher than that of the single half-circle, given that both half circles are radiating constructively. Moreover, at *f* = 12 THz, the peak value of the radiated field decreases due to an out of phase radiation, i.e. the radiation coming out of the two circles add destructively. In the next section, a new structure will be developed to exploit the fact that a change of frequency can achieve coherence.

Fig. 24 shows a top-view of the simulated structure. The main idea is to achieve a constructive radiation of the two-half circles. As a result, a higher radiated power or equivalently higher radiation efficiency can be attained. In order to do this, a transmission line of distance *d* is inserted between the two half-circles. By changes the distance *d*, the phase difference of the EM-waves propagating along the two half circles is controlled. In this manner, a constructive or a destructive radiation can be achieved. It is important to mention that the radiated power will be function of frequency and the distance *d* when keeping all the other parameters fixed.

FDTD simulations were carried to obtain the radiation efficiency as a function of the distance *d*. Fig. 25 shows the results, where one observes that a change of the distance *d* affects both the amount of the radiated power and the frequency at which the maximum value of radiation occurs. Also, *d* equals 2R gives a very high radiation efficiency at *f* = 18 THz (almost all the input power is lost into radiation).

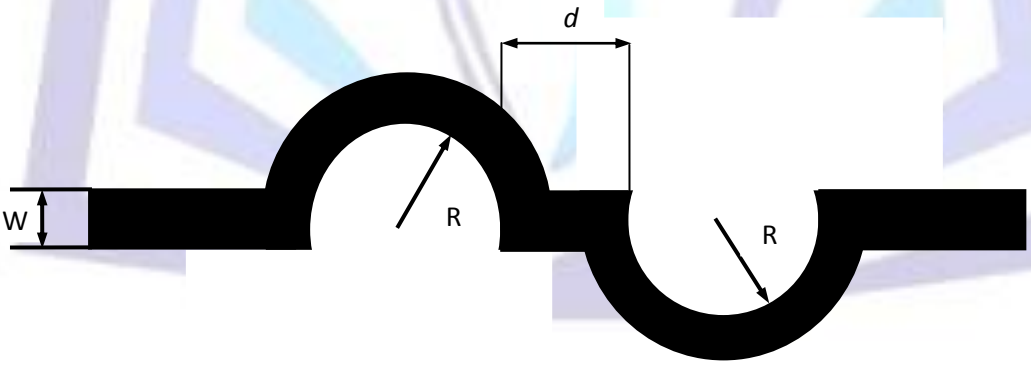

Fig. 24. Top-view of two half-circles separated by a distance *d*. R = 4 μm and W= 2 μm.

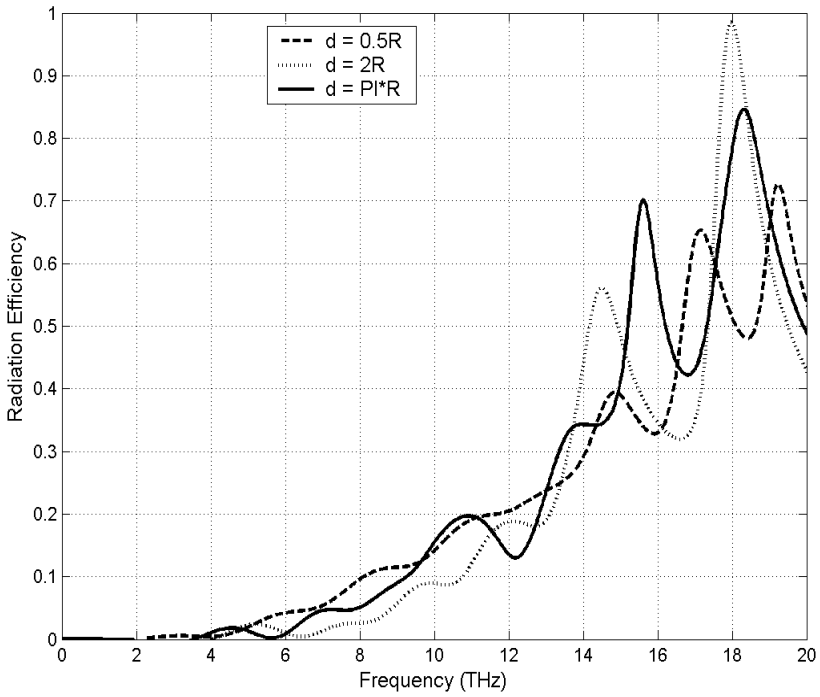

Fig. 25. Radiation efficiency curves for different values of the separation distance *d*.

VI. Conclusions And Future Research

This paper presents several possibilities for coherent radiation in the THz range based on micro undulator ideas. There are several interesting assumptions that we have made and now attempting to justify that includes such things as the low energy limit of SR, and the differences between quantum and classical pictures in this domain e.g. we need to study mobility and whether a scattering event during radiation takes it out of the classical SR picture. It has been argued that bound implementations have a number of advantages including costs based on using standard IC techniques as opposed to current macro FELs. Simple scaling needs to be checked, i.e. radiation may not be scale invariant. A related question concerns the frequencies allowed when we add a mirror symmetric combination above the structure in Fig. 1 or Fig. 8 since this will certainly serve as a high pass filter in the case of structures such as Fig. 8.

Appendix

Control of the 6-dimensional phase space of a particle or photon beam begins with production and proceeds through every subsequent step until extraction and use. A quantity that best represents the fully invariant 6-D phase space for linear, time independent systems is the normalized brightness:

$$B_n^6 = \frac{\mathrm{N}}{\varepsilon_{\mathrm{nx}}\varepsilon_{\mathrm{ny}}\sigma_t\sigma_\omega} \tag{11}$$

where N is the number of quasi-particles (electrons or photons) in a bunch, ε_{nx} and ε_{ny} are the transverse, normalized emittances and σ_z and $\sigma_{\square}$ are the corresponding longitudinal parameters - the bunch's rms length and energy spread. For photons, we can simplify this to:

$$B_n^6 = (4\pi)^2 \frac{\mathrm{N}_\gamma}{\lambda^2\sigma_t\sigma_\omega / \varpi}\eta \tag{12}$$

where an intense source can be defined as one with $\tilde{N}_{\square}{}^{3}$ »1. We need to extend this discussion on brightness to point out that it is not an inherent characteristic of the beam but of its focus and containment environment…

Acknowledgement

This work was supported by the US Department of Energy under contract *DE-ACO3-76SF00515.*

References

[1] Y. Hussein and J. Spencer, “Novel possibilities for coherent radiation sources,” in *Proc. IEEE MTT-S Int. Sym. Dig*., 2004, pp.151-154.

[2] Y. Hussein and J. Spencer, “Hybrid FDTD analysis for periodic on-chip terahertz (THz) structures,” in *Proc.* IEEE/ACES International Conference *Sym. Dig*., 2005, pp.797-800.

[3] Yasser A. Hussein and James E. Spencer, “An efficient 95-GHz, RF-coupled antenna,” in IEEE PAC Dig., 2007, pp. 1314 – 1316.

[4] Yasser A. Hussein and James E. Spencer, “Radiative characteristics of on-chip terahertz THz structures,” in IEEE AP-S Int. Antennas and propagation Symp. Dig., 2005, pp. 250 – 253.

[5] Peter H. Siegel, “Terahertz Technology”, *IEEE Trans. Microwave Theory Tech*., vol. 50, No. 3, Mar. 2002.

[6] Waters, J.W., et al., “The Earth observing system microwave limb sounder (EOS MLS) on the aura Satellite”, *IEEE Trans. Geoscience and Remote Sensing*, vol. 44, No. 5, pp. 1075 – 1092, 2006.

[7] Cooper, K.B., *et.al*., “Penetrating 3-D Imaging at 4- and 25-m Range Using a Submillimeter-Wave Radar”, IEEE Trans. Microwave Theory Tech., vol. 56, No. 12, pp. 2771 – 2778, 2008.

[8] Cooper, K.B., et.al., “THz Imaging Radar for Standoff Personnel Screening”, *IEEE Trans. Terahertz Science and Tech.*, vol. 1, No. 11, pp. 169 - 182 , 2011.

[9] Cooper, K.B., *et.al*., “A High-Resolution Imaging Radar at 580 GHz”, *IEEE Microwave and Wireless Component Letters.*, vol. 18, No. 1, pp. 64 - 66 , 2008.

[10] Peter H. Siegel, “Terahertz Technology”, *IEEE Trans. Antennas and Propagation*, vol. 58, No. 6, pp. 2957 – 2965, 2007.

[11] Maestrini, A., *et.al.*, “Design and Characterization of a Room Temperature All-Solid-State Electronic Source Tunable From 2.48 to 2.75 THz”, *IEEE Trans. Terahertz Science and Tech.*, vol 2, No. 11, pp. 177 - 185 , 2012.

[12] Popov, M., *et.al.*, “Sub-Terahertz Magnetic and Dielectric Excitations in Hexagonal Ferrites”, *IEEE Trans. Magnetics*, vol 47, No. 2, pp. 289 - 294, 2011.

[13] Wang, Y. ., *et.al.*, “Broadband Terahertz Left-Hand Material With Negative Permeability for Magnetic Response”, *IEEE Trans. Magnetics*, vol 47, No. 10, pp. 2592 - 2595, 2011.

[14] Gerald J. Wilmink ., *et.al.*, “Invited Review Article: Current State of Research on Biological Effects of Terahertz Radiation”, *Journal of Infrared, Millimeter, and Terahertz Waves,* vol 32, No. 10, pp. 1074-1122, 2011.

[15] Kumud Ranjan Jha and G. Singh “Analysis and design of enhanced directivity microstrip antenna at terahertz frequency by using electromagnetic bandgap material”, *International Journal of Numerical Modeling,* vol 24, No. 5, pp. 410–424,2010.

[16] S. James Allen, “Terahertz Dynamics in Semiconductor Quantum Structures”, *27th Int’l. Conf. IR and Millimeter Waves*, Sept. 2002.

[17] D. M. Sheen, *et al*., “Application of the three-dimensional finite-difference time-domain method to the analysis of planar microstrip circuits,” *IEEE Trans. Microwave Theory Tech.,* vol. 38, pp.849-857, July 1990.

[18] Wanill Ha, *et al.*, “Miniaturization Techniques for Accelerators”, *2003 Part. Accel. Conf*., May 2003.

[19] Julian Schwinger, “On the Classical Radiation of Accelerated Electrons”, *Phys. Rev.*, June 1949.

[20] S.J. Smith and E.M. Purcell, “Visible Light from Localized Surface Charges Moving across a Grating”, *Phys. Rev.* 92, Aug. 1953.

[21] C. Guo et al., “Structural Phase Transition of Aluminum Induced by Electronic Excitation”, *Phys. Rev. Lett* 84, May 2000.

[22] C. Weiss et al., “Generation of tunable narrowband surface-emitted THz-radiation in periodically poled Lithium Niobate”, *Opt. Lett.* 26, 2001.